Experimental validation of the MODTRAN 5.3 sea surface radiance model using MIRAMER campaign measurements

Vincent Ross,[1,*] Denis Dion,[2] and Daniel St-Germain[2]

[1] *AEREX Avionic Inc.,*
324, av. Saint-Augustin Breakeyville, Qc, Canada, G0S 1E1

[2] *Defense Research and Development Canada, Valcartier,*
2459 boul. Pie-XI Val-Blair, Qc, Canada, G3J 1X5

[*] *Corresponding author: vross@aerex.ca*

Radiometric images taken in mid-wave and long-wave infrared bands are used as a basis for validating a sea surface BRDF being implemented into MODTRAN® 5 [1]. The images were obtained during the MIRAMER campaign that took place in May 2008 in the Mediterranean Sea near Toulon, France. When atmosphere radiances are matched at the horizon to remove possible calibration offsets, the implementation of the BRDF in MODTRAN produces good sea surface radiance agreement, usually within 2% and at worst 4% from off glint azimuthally averaged measurements. Simulations also compare quite favorably to glint measurements. The observed sea radiance deviations between model and measurements are not systematic, and are well within expected experimental uncertainties. This is largely attributed to proper radiative coupling between the surface and the atmosphere implemented using the DISORT multiple scattering algorithm.

OCIS codes: 010.4450, 010.5620, 030.6600, 110.3080.

1. Introduction

The reflectivity of the sea surface plays an important physical role in the maritime environment. It affects how radiative energy is exchanged between the sea surface and the atmosphere, and therefore influences the energy balance of the entire maritime atmosphere

system. Because of its elevated content in highly scattering aerosols and water vapor, the air mass above the surface scatters or absorbs some of the radiation, making the multiple exchanges back and forth between the water surface and the atmosphere even more important and difficult to model. Good knowledge of the radiative properties of the surface and maritime atmosphere is crucial in remote sensing applications and for the study of sensor systems in or above maritime environments.

For these reasons, any application requiring radiative transfer calculations in a maritime context necessitates propagation models that include a proper sea surface BRDF (Bidirectional Reflectance Distribution Function) in order to describe the strong directional nature of the reflectivity of the sea surface. Furthermore, because of the radiative exchanges that occur between the surface and atmosphere, the model must adequately couple the surface reflectivity with the atmospheric light field. This can naturally be done by using the surface BRDF as a lower boundary condition in a multiple scattering algorithm. Unfortunately, this coupling is sometimes ignored. One of the reasons is that for a single radiative calculation, potentially hundreds of BRDF calculations are required in order to account for all the possible reflection and scattering geometries. This can take a tremendous toll on computational times, especially since, until recently, all but the roughest approximations of the sea surface BRDF were slow to evaluate.

MODTRAN [1, 2], probably the most widely used radiative transfer code, did not contain any sea surface BRDF model up to version 5. Since the BRDF models it did contain were close enough to a Lambert reflector (isotropic), coupling with the multiple scattering algorithm had no major impact and was left out.

Recent efforts have been made to incorporate within MODTRAN an analytical expression of the specular sea surface BRDF developed at DRDC Valcartier in Canada [3, 4]. While relatively quick to evaluate, the DRDC sea surface BRDF expression possesses features such as bistatic wave shadowing which increases its physical correctness. Measurements obtained during the MIRAMER campaign conducted in May 2008 in the Mediterranean Sea by France with the participation of Canada provide the opportunity for validating the sea surface radiance model implemented in MODTRAN.

In this paper, we present the models involved, describe the campaign and the consequential measurements, and present comparisons of measurements and simulations. Possible causes of discrepancies between measurements and computations are discussed and assessed. The accuracy of the model and its limitations are evaluated and future development and validation are suggested.

2. Sea surface BRDF coupling to DISORT in MODTRAN

In order to properly model the reflected radiance off the surface, one must not only take into account the directionality of the surface reflectance, but also that of the impinging radiation. Because of the highly directional nature of the sea surface BRDF, this is especially important and affects both atmospheric and surface radiances. In MODTRAN 5, directional surface-atmosphere radiative coupling is done most naturally and thoroughly by using the surface BRDF as a lower boundary condition to the N-stream multiple scattering algorithm DISORT [5]. This capability is already built into the DISORT implementation in MODTRAN, as it accepts azimuthal Fourier moments of the BRDF as input [6]. The analytical nature of the Ross et al. sea surface BRDF model makes it ideal for a computationally intensive purpose such as multiple scattering calculations, while still retaining important features such as wave hiding and shadowing. An overview of the theoretical details concerning the sea surface BRDF can be found in Appendix A.

Because the surface emits and reflects energy back into the atmosphere, this energy can in turn be scattered back into the line of sight of the sensor. The impact of BRDF coupling on path (atmospheric) radiances can be assessed by comparing simulations with a coupled sea surface BRDF to simulations considering a Lambert reflector with equivalent albedo as the lower surface (the approach implemented previously in MODTRAN). Computations were performed in the visible spectrum over a 40 degrees field of view with a relatively hazy atmosphere. In order to obtain significant path radiance values over the entire field of view, the sensor is placed at 250 meters in altitude with a horizontal elevation. The DISORT multiple scattering is used with 16 streams. The percentile differences in path radiance between both coupling modes are plotted in Fig. 1 on the right, along with the corresponding synthetic color image for reference on the left. The relative differences on path radiance in these particular circumstances surpass 45%. Even far from the sun glint region, the differences still remain over 25% for most of the down looking paths. The errors stem mainly from the strong directionality of the surface reflectance, producing a more directional scattered light field. Such differences are large enough to significantly affect outcomes in many applications such as target detection range estimations for airborne sensors, leading to erroneous results. The errors become negligible only as the lines of sight move close to the sun's position, since single scattering dominates in these geometries. It is to be expected that calculations in IR bands using a Lambert surface instead of the full BRDF would also show errors, although to a lesser degree than in the visible, since the thermal emissions in these bands also have a more directional behavior than with a Lambert surface.

3. Measurements

The MIRAMER (from the French: Mesure Infrarouge du Rayonnement de la MER meaning Infrared Measurements of SEA Radiation) campaign was held from the 13^{th} to the 28^{th} of May 2008 in the Mediterranean Sea in the vicinity of Toulon, France. The purpose of the campaign was to gather radiometric measurements as well as environmental data in order to validate maritime background and target signature models. Participants included a number of organizations in France and DRDC in Canada.

During the campaign, the IFREMER (Institut Français de Recherche pour l'Exploitation de la MER) ship *Atalante* provided by the SHOM (Service Hydrographique et Océanographique de la Marine) was used to gather off-shore measurements between the 18^{th} and the 28^{th} of May. The ship had on its board a number of instruments to measure meteorological data, solar fluxes, atmospheric visibility as well as sea temperature and salinity. Radiosonde measurements were taken at least a few times each day. The French organization ONERA had on board two Jade model Cedip (now known as Flir ATS) infrared cameras which they used to take imagery of the sea surface near the horizon with 8 by 11 degrees (240 by 320 pixels) field of views in mid-wave and long wave infrared bands. The cameras were mounted 13 meters above the water level.

The mid-wave camera operates in the mid-infrared, from 3.4 to 5.5 microns. Hereafter this band is often referred to as BII. In order to prevent pixel saturation in sun glint images a narrower and more absorbing filter was used. This filter reduces the spectral range to the 3.93 to 4.14 micron band (dotted line on Figure 2), with a maximum in transmission of about 80%. Without the filter, its spectral response is shown with the full line in Figure 2.

The long-wave CEDIP camera provides images further into the infrared, with its sensitivity centered on 8.6 μm (hereafter referred to as band BIII). A filter reducing the spectral rage to 8.19 to 8.96 microns was used for all measurements presented here (Fig. 3).

Images taken with both cameras are calibrated pixel by pixel using a series of 4 images of onboard constant temperature blackbodies. These images are taken between each measurement with the blackbodies filling the entire field of view. Pixel data is then converted to measured integrated radiance ($W/m^2/ster$) in the filter band and renormalized as if the filter had a square unit response. Images with no glint use black bodies of 15, 20, 25 and 30°C, while glint images are calibrated with 20, 25, 100 and 125°C blackbodies to accommodate for the greater dynamic range of the measurements.

Off glint measurements made on the 23^{rd} of May were selected for the analysis. The 23^{rd} was mostly a clear day except for some presence of clouds around noon and some scattered clouds during the rest of the day. The benefit of this is twofold. First, it minimizes some of the complexities and therefore sources of errors associated with modeling clouds. Secondly, it provides measurements under a large number of solar geometries, with solar elevations

ranging from about 16 to 47 degrees. The 23rd also offers an appreciable wind speed span.

Not only were the skies clear, but the measured visibilities were in excess of 25 km for all cloudless periods. On one hand, this should minimize the errors due the modeled aerosols on the simulated images (more is said on this subject in section 5.B), and on the other hand, this lets the cameras measure sea radiances up closer to the horizon before atmospheric scattered and emitted radiance becomes the dominant source of energy.

The wind speed for the period ranges from just below 1 m/s to nearly 7 m/s, which gives us a good validation range. Also, three radiosondes were launched during the day, covering most of the period when the cameras were functioning. These radiosonde profiles were interpolated to yield atmospheric profiles for the entire day. Air and sea temperatures did not vary much during the day, which most likely indicates that their spatial variability along the lines of sight was also kept to a minimum.

Many images were taken throughout the day on the 23rd. For the purpose of this paper, a number of selection criteria were established in order to narrow the selection to an appropriate number. First and foremost, all selected images were required to have the horizon visible in the field of view for calibration purposes (see section 5.A). All measurements taken during cloudy periods, mostly occurring in the hours around noon, were excluded. Furthermore, cases were wind speed was above 1.5 m/s were chosen, since for very low wind speeds surface slope variance models are more tentative and true water surface (skin) temperature over the range of interest can differ significantly from measurements. Low wind speeds also produce a strongly anisotropic BRDF requiring more DISORT streams and longer computational times. Finally, cases with low wind speed variances over 2 minute periods were preferred.

No good solar glint images were captured on the 23rd, with only partial glint patterns captured by the cameras and no image including the horizon. Because of this, good quality solar glint measurements obtained on the 22nd and 28th of May were selected. Although skies were reported as being somewhat veiled on the morning of the 28th, it is possible to compensate by incorporating cirrus clouds in the calculations as described in section 6.

Finally, all measurements were taken at more than 67 km from the coast. This minimizes the influence of the coast on the sea state, and prevents the coastline from contaminating the images close to the horizon. Table 1 presents the significant modeling parameters for selected cases.

4. Simulations

All simulated images are generated using MODTRAN 5 version 3 (developmental version containing the DRDC BRDF model). MODTRAN runs are done for each azimuth and elevation on an adaptive grid that places more grid points around the horizon and near the sun and glint pattern. Linear interpolation can then be used in between grid points to obtain

radiance profiles on the same grid as the MIRAMER measured images.

As much as possible, environmental parameters that must be input into MODTRAN are taken from in-situ measurements made on board the ship. In order to obtain greater accuracy on the atmospheric component of the modeled radiance, vertical atmospheric profiles of thermodynamic and optical properties are modeled more finely using measured quantities. This is especially important in the lower atmosphere where the lines of sight gather most of their atmospheric radiance.

Meteorological profiles (temperature, pressure, relative humidity, wind speed) in the lower 10 meters are finely modeled based on the Monin-Obukhov similarity theory using the DRDC Valcartier model [7]. Above the modeled profile, meteorological data taken from radiosondes launched from the ship at 7h20, 12h24 and 18h26 are interpolated at the time each individual image was obtained. For images captured earlier than the first sonde launch, the earliest measurement is used (7h20). The MODTRAN mid-latitude summer profile is used above radiosonde profiles up to the top of the atmosphere (120 km).

Aerosol optical properties in the surface layer are modeled using the Mediterranean aerosol model MEDEX developed in France [8], as implemented in the DRDC AeroProC computer model [9]. In AeroProC, the NOVAM model [10] is used to describe aerosol profiles up to altitudes of 500 m to 2 km depending on the conditions. As necessary, the profile is completed using the MODTRAN NAM maritime aerosol model [11] up to about 2 km. Aerosol extinctions are scaled using the visibility measured on board the *Atalente*. Any visibility greater than 50 km is considered outside the sensitivity range of the instrument, so visibilities are capped at 50 km. Scattering and extinction coefficients, as well as phase functions generated by the AeroProC model are fed into MODTRAN 5 using the new SAP (Spectral Aerosol Profile) input interface.

Sun elevation and azimuth data was not gathered on site, but can be readily calculated from the ship's GPS position. Correction on the sun elevation due to atmospheric refraction is applied using Saemundsson's formula [12] and is adjusted to wavelength. The deviation from the unrefracted sun position is below 0.1 degrees with the considered sun elevations.

Sea surface slope variances required as input to the MODTRAN 5 BRDF implementation are obtained from wave number integration of the Elfouhaily et al. [13] wave spectrum according to

$$\begin{aligned} \alpha &= \frac{1}{2}\int_0^\infty k^2 \mathrm{M}_E(k)dk, \\ \beta &= \frac{1}{4}\int_0^\infty k^2 \mathrm{M}_E(k)\Delta_E(k)\,dk \end{aligned} \tag{1}$$

where k is the wave number, $M_E(k)$ is the omnidirectional Elfouhaily et al. spectrum cal-

culated using the wind speed measured 10 m above the mean sea surface, and $\Delta_E(k)$ is a term in their angular spreading function which describes how different parts of the spectrum (notably the gravity and capillary wave domains) vary according to wind direction.

From equations 1, the upwind (σ_x^2) and crosswind (σ_y^2) slope variances (Fig. 4) are then obtained with

$$\sigma_x^2 = \alpha + \beta, \quad \sigma_y^2 = \alpha - \beta. \tag{2}$$

All simulations are run using DISORT with 16 streams (which are basically quadrature points). In some cases 8 streams might have sufficed, especially in cases with high wind speeds where the BRDF is more spread out, but 16 streams was used nonetheless in all simulations for consistency.

5. Error factors

Before comparing measurements and simulations, it is instructive to discuss the possible sources of differences, may they be due to the sea surface BRDF model or not, as well as steps taken to eliminate some of them when possible.

5.A. Experimental uncertainties

As with any experimental campaign set up in natural environments, not all factors can be controlled, and not all parameters measured. For example, we can expect some unmonitored variability of meteorological parameters along the distance covered by the measured images (the horizon is about 20 km from the sensor). Air and sea surface temperatures were somewhat stable during the day, but sharp variations of around 1°C were sometimes observed in relatively short time spans (1 hour) as the ship changed position. This suggests that variations with distance of about 1°C are possible. Wind was a bit gusty and variable during the day. Two minute averages of instantaneous wind speed measurements were used for the simulations diminishing the impact of the gusts. Nonetheless, it is likely that variation with distance accounts for some discrepancies between calculations and measurements.

Another potential cause of uncertainty steaming from the measurements is the surface temperature. The thermometer, although quite accurate, is located below the surface of the water. Even at a relatively shallow depth, the difference between the measured temperature (called bulk temperature) and the temperature measured by a radiometric instrument off the surface (called skin temperature) can easily reach plus or minus 0.5 to 1°C, with a cooler skin at night due to evaporation, and a warmer skin in the day due to solar heating [14]. This is because in the infrared bands and at grazing angles, the measured radiance is emitted at very shallow depths (below 100 μm, see Fig. 4 in [14]), since water extinction is larger in these spectral bands. These differences are likely to be greater at low wind speeds because of increased turbulent mixing at higher wind velocities.

Other sources of uncertainty will mostly affect solar glint measurements. The main one being the presence of scattered clouds or cirrus since they can reduce the incident solar irradiance considerably. The actual value of incident direct solar radiation is difficult to determine since the pyranometers measured both diffuse and direct contributions. Solar irradiance based measurements of atmospheric optical depth collected in Toulon are used instead. Furthermore, the instrument meant to measure the exact heading (azimuth) of the cameras failed. To compensate, the ship heading was used to calculate the instrument azimuth. This should produce good enough values of measurements outside glint patterns, but small deviations might have large effect on glint measurements because of the rapid falloff in radiance of glint patterns.

Finally, the calibration process can also introduce some errors. Drifts in temperature (up to 5% in radiance) or small surface inhomogeneities in the temperature of the reference blackbodies can occur, producing absolute shifts in the measured radiances and affecting the dynamic range (compressing or stretching the radiance values). This is especially true for BIII images where the dynamic range of the 25°C calibration blackbody images is close to that of the images themselves. Overall, systematic biases of up to 20% can be potentially introduced into the measurements from calibration only. Dispite the great care that was taken in order to calibrate each image individually, there is a general consensus amongst all parties involved in this study that such a bias was introduced in most measurements trough calibration. One reason is that errors are consistent throughout any given profile, equally affecting sky and sea radiances whose temperatures are measured independently. In order to remove this bias, radiance values at the horizon on both measured and simulated images are matched by shifting simulation results. In the majority of cases, the shift represents less than 5% of the measured radiance values; well within accepted calibration uncertainties. Since the main purpose of this paper is the validation of sea radiance calculations, there is some rationale in matching horizon radiances which represent only atmospheric contributions. This has the benefit of also reducing some of the errors introduced by uncertainties in the measurement of atmospheric parameters, while maintaining the morphological aspect of the simulated radiance profiles which are a critical aspect of this validation.

5.B. Modeling errors

Quantities either intervening in the radiance model or used as input to the BRDF are based on models that can have intrinsic errors or uncertainties associated to them. Added to the wind speed variability mentioned in section 5.A is the uncertainty on the chosen theoretical slope variance model required by the BRDF. For example, the Elfouhaily et al. model used here can deviate from the classic Cox and Munk model by as much as 80% with wind speeds ranging between 1.5 and 5 m/s. Coupled with 25% variations of wind speed observed during

the two minute averages we estimate that the uncertainty on slope variances can reach 100%. The impact on such an uncertainty is shown in Fig. 5 where it is applied on the 8.19 to 8.96 μm ATAL 108 case. Because of the low wind speed on this particular case (about 1.4 m/s) and high wind variance (0.4 m/s), the effect is amplified, so this should be viewed as a worst case scenario. Because of this, the case was excluded from the analysis in section 6.

At shallow elevation angles, a large fraction of the observed radiance comes from atmospheric contributions. This is partly because at grazing angles reflection is more efficient (Fresnel) so more of the sky radiance is reflected towards the camera. This is compounded by the fact that the distance between the surface and camera is much greater, up to 20 km near the horizon. Aerosol scattering and thermal emission are thus important components that must be accurately taken into account in the atmospheric radiance calculations. Although using a state of the art aerosol model developed especially for the Mediterranean certainly helps, many parameters escape our control. For example, desert or urban aerosol properties which vary greatly day by day depending on wind direction might differ from the MEDEX predictions.

There is also the matter of scattered clouds. Even if a measurement period was logged as clear, the presence of a few thin scattered clouds near the horizon can alter the surface reflected radiance considerably. This situation cannot be modeled by 1D models like MODTRAN which do not consider horizontal variations and inhomogeneities.

Finally, subsurface scattering and multiple reflections are not considered in the DRDC BRDF model. Although in the spectral range considered here subsurface scattering should be negligible because of water absorption, Ross et al. [4] estimated that no more than 2 to 3% of sea surface radiance can come from multiple scattering,with the largest errors occurring at high wind speeds, low sun elevations and near horizontal detector orientations.

6. Computational results and Discussion

All comparisons between non-glint measurements for both BII and BIII bands and MODTRAN computations are shown in chronological order (from top to bottom) in Fig. 6. Experimental curves are shown with continuous lines, while simulated curves are dotted. The shift applied to the simulated curve in order for the radiances at the horizon to match is indicated in each figures legend. All curves are obtained by averaging experimental and simulated images in azimuth for a large section excluding the first and last 50 pixels. This is done since some measured images exhibit signs of calibration errors on one of their edges, probably caused by having the calibration blackbodies not fill the image frame entirely. Averaging the images in this way also removes some of the variability in the experimental images, making the comparison with MODTRAN easier. Percentile differences between simulated and measured radiances are plotted below each figure. Note that there seems to be a slight upward

bias in BII measured images which can be attributed to the calibration procedure.

In spite of this slight bias, the BRDF model implemented in MODTRAN produces fairly good results overall in both bands. No significant systematic deviations in both curve morphology and absolute values are observed. The worst deviations are encountered in the morning measurements, and remain below 4% (or about 2.5°C in apparent temperature), while most divergences are within 2% (below 1.25°C in apparent temperature). Note that errors seem larger on the plots because of the narrow range of the radiance axes. As the day progresses, the deviation seems to drift from simulations overestimating the radiance to matching it almost exactly for case 107 BII, and then undervaluing measurements. This is more obvious near the horizon in the BII images. As an error in the BRDF model would more likely produce systematic errors, environmental factors are thus more likely to blame. There is a good chance that quantities such as surface temperature differ from the value used as input near the horizon, 20 km from the measurement site. Air-sea temperature differences also went from negative in the morning to positive in the afternoon. This, compounded with low wind speeds in the morning and late in the afternoon, might give rise to differences between measured bulk and actual skin temperatures which could also be to blame. A downward bias in the morning and an upward bias of measurements is certainly consistent with a morning cool skin and a warmer afternoon skin temperature. Air stability can also affect the aerosol characteristics [15, 16] as well as sea surface slope statistics [17, 18].

Cases 107 and 109 can also give insight into possible causes of deviations since measurements are available in both bands. Measurements were simultaneous, and simulations use exactly the same environmental input. The BRDF model itself is not expected to have spectral variability other than small differences due to the well characterized Fresnel reflection coefficients. Therefore, all else being equal, calibration uncertainties likely have a big role to play in observed differences. Errors due to calibration are also obvious when comparing the ATAL 89 (trial 1116) BIII case to the other BIII measurements, where the apparent temperature of the entire profile is at least 10 degrees lower with no physical basis. Note that this is also the case where the worst deviations between measurements and simulations occur.

Unfortunately, at the time the solar glint measurements were made on the morning of the 28^{th} of May, the instrument measuring aerosol visibility did not function. The visibility can be approximated empirically from the instantaneous wind speed and the 24 hour averaged wind speed according to the NAM aerosol model algorithm [11]. The value obtained is about 18.5 km.

Personal logs from that morning also indicate a veiled sky suggesting the presence of a cirrus cloud layer. In order to estimate the cloud optical depth, version 2 level 1.0 (direct sun, unscreened for cirrus clouds) aerosol optical depth (AOD) measurements from the nearby

Toulon AERONET station are used. AOD values are extrapolated to the time the glint image was captured (only about 12 minutes before the first AOD measurement). Values are also extrapolated to the center of the filter band using an Angstrom exponent of -0.05 (the value found between 0.675 and 1.02 μm). In order for the sum of aerosol and cirrus cloud optical depth to match the value obtained from AERONET, a layer of standard MODTRAN cirrus of 1.8 km thickness is required. With this thickness, direct solar irradiance is reduced by a factor of about 10.

In order to compare measured glint measurements to MODTRAN simulations, a vertical and a horizontal profile were obtained for both measurements and simulations of case ATAL 145. The vertical profiles (Fig. 7 A) are a result of averaging a 100 pixel wide band centered on the glint pattern (region A on top pane of Fig. 7). Horizontal profiles (Fig. 7 B) are obtained from averaging a 170 pixel high region (region B on top pane of Fig. 7). The simulation is shifted by -0.05 W/m2/ster in order for radiances at the horizon to match.

Good agreement between measured and simulated sun glint radiance values is observed. The crude approximation in aerosol visibility might be responsible for the slightly sharper drop-off in the vertical radiance profile closer to the horizon compared with the measurements. The excellent match of simulated and measured width of the glint pattern suggests that the slope variance model closely mirrors the actual values. Differences between simulation and measurements are also plotted. The mean differences ($\overline{err}$) on the vertical and horizontal profiles are 6.32% and 1.87% which is small compared to the standard deviations of the difference curves (σ_{err}) of 32.75% and 11.11% respectively. This means that there is no significant systematic deviation of the simulations from the measurements.

Unlike the morning of the 28$^{\text{th}}$, the 22$^{\text{nd}}$ of May started out with a clear sky and a very good visibility. Similar plots averaging the vertical profile on 140 pixels, and on 200 pixels for the horizontal profile were produced and are presented in Fig. 8. Wind speed was 5.6 m/s, which produces a good match to the data, although slightly more peaked near the center of the horizontal profile and near the horizon in the vertical profile. Ross et al. [4] found an effective increase in slope variance by a factor of 1.5 up to the horizon because of shadowing effects. By applying the correction, the agreement between measurements and simulation is increased for both horizontal and vertical profiles. This correction does not seem necessary for case ATAL 145, likely because of the much lower wind speed (although no wind speed dependence was found in the Ross et al. paper).

Similarly but to a higher degree than the case of the 28$^{\text{th}}$ (ATAL 145), the falloff near the horizon on the vertical profile happens closer to the horizon and is more pronounced in the simulation. Although this could be the result of approximations used in the BRDF, it can also be attributed to an underestimation of the aerosol load near the surface in the simulations.

7. Conclusion

The MIRAMER campaign conducted in the Mediterranean Sea provides imaging data well suited for validating sea radiance models contained in a recent version of MODTRAN, which includes a sea surface BRDF.

An attractive feature of the implementation in MODTRAN is that the sea surface BRDF is radiatively coupled with the atmosphere when multiple scattering options are enabled, This coupling is especially important since the sea surface exhibits a very anisotropic reflectance, as demonstrated by the increased accuracy of apparent surface radiance simulations. To accomplish that, the atmospheric light field must be correctly modeled, since the atmosphere's energy is not only reflected against the surface towards the sensor but also back into the atmosphere, adding to the total radiance along the optical path between the camera and the sea surface. Proper modeling of the atmospheric light field is only possible if the environmental parameters are well characterized.

In this validation effort, uncertainties related to the characterization of the environment (thermodynamic profiles, aerosols, etc.) are thought to be the principal source of errors. Additional factors to consider are the limited calibration accuracy, the possible difference in bulk versus skin surface temperature and the likelihood of horizontal variability not taken into account in MODTRAN. Nonetheless, simulations faired quite well; no systematic deviations between simulations and measurements were observed, while relative deviations remain below 4%. This suggests that errors steaming directly from the BRDF and the approximation used therein are small enough to be buried by the more important environmental and experimental factors.

Since a sea radiance computation can only be truly validated in a natural setting, it is impossible to completely eliminate sources of uncertainty encountered here. One solution might be to better characterize the entire sky hemisphere radiance distribution by using dome mirrors or fisheye lenses. Although MODTRAN cannot handle inhomogeneities that would be encountered, these would permit better analysis of the discrepancies between model and measurements. Another way around some errors would be to use radiometric skin temperatures in the simulations, or at least to attempt to model them from bulk measurements of air and sea temperatures.

Appendix A

The bidirectional reflectance distribution function in its reciprocal and normalized form is usually described as the ratio of radiance L_r of the surface in the receiver direction $\mathbf{\Psi}_r = (\theta_r, \phi_r)$ and the source irradiance incident on the surface $E_s \cos\theta_s$ from source direction

$\boldsymbol{\Psi}_s = (\theta_s, \phi_s)$

$$f(\boldsymbol{\Psi}_s, \boldsymbol{\Psi}_r) = \frac{\pi L_r(\boldsymbol{\Psi}_r)}{E_s(\boldsymbol{\Psi}_s)\cos\theta_s}, \tag{A1}$$

where θ_s is the angle between the source and the average surface normal (zenith angle for a horizontal surface) and ϕ denotes the azimuth angles as in Fig. 9. Although there are different conventions for normalizing the BRDF, the π factor was chosen here since it is the convention used in DISORT [5] and MODTRAN [6].

A statistical specular BRDF model is proportional to the probability that the geometrical configuration, or slope vector $\boldsymbol{\zeta} = (\zeta_x, \zeta_y)$ of the surface, can produce a specular reflection from the source to the receiver

$$f(\boldsymbol{\Psi}_s, \boldsymbol{\Psi}_r) \propto p(\boldsymbol{\zeta}), \tag{A2}$$

where p is called the occurrence probability density function (PDF) since it represents the probability of the reflection geometry occurring on the surface. From aerial photographs of sun glint off the sea surface, Cox and Munk [19, 20] found that the PDF was well fitted by a Gram-Charlier expansion whose first order term is the Gaussian

$$p_0(\boldsymbol{\zeta}) \approx \frac{1}{2\pi\sigma_x\sigma_y} \exp\left\{-\frac{1}{2}\left(\frac{\zeta_x^2}{\sigma_x^2} + \frac{\zeta_y^2}{\sigma_y^2}\right)\right\}, \tag{A3}$$

where ζ_x and ζ_y are the upwind and cross wind slopes, and σ_x^2 and σ_y^2 are the upwind and crosswind variances.

Additional terms are needed to correct for kurtosis (peakedness) and skewness,

$$\begin{aligned} p(\boldsymbol{\zeta}) \approx\ & p_0(\boldsymbol{\zeta})\left\{1 - \frac{1}{2}c_{21}\left(Y^2-1\right)X - \frac{1}{6}c_{03}\left(X^3 - 3X\right)\right. \\ & + \frac{1}{24}c_{40}\left(Y^4 - 6Y^2 + 3\right) + \frac{1}{4}c_{22}\left(Y^2-1\right)\left(X^2-1\right) \\ & \left. + \frac{1}{24}c_{04}\left(X^4 - 6X^2 + 3\right)\right\}, \end{aligned} \tag{A4}$$

where

$$X = \frac{\zeta_x}{\sigma_x}, \quad Y = \frac{\zeta_y}{\sigma_y}. \tag{A5}$$

The Cox & Munk skewness expansion coefficients in equation A4 are given by

$$c_{21} = 0.01 - 0.0086U, \quad c_{03} = 0.04 - 0.033U \tag{A6}$$

while the kurtosis coefficients are

$$c_{40} = 0.40, \quad c_{22} = 0.12, \quad c_{04} = 0.23. \tag{A7}$$

The Gram-Charlier series representation of the sea slope PDF has rarely been disputed in the literature (Liu et al. [21] and Plant [22] are a few exceptions).

From the expression for the occurrence PDF of the sea surface, a statistical BRDF can be derived. Ross et al. [3] developed an analytical approximation to the sea surface BRDF that is applicable to a height-slope uncorrelated quasi-Gaussian surface. The BRDF can be expressed in the form of equation A1 as

$$f\left(\mathbf{\Psi}_s, \mathbf{\Psi}_r\right) = \frac{\pi r\left(\mathbf{\Psi}_s, \mathbf{\Psi}_r\right) q_{vn}\left(\mathbf{\Psi}_s, \mathbf{\Psi}_r\right)}{4 z_n^3 (\mathbf{U}_n \cdot \mathbf{U}_r) \cos\theta_s}, \tag{A8}$$

where q_{vn} is the normalized visible interaction PDF and is related to the occurrence PDF by

$$q_{vn}\left(\mathbf{\Psi}_s, \mathbf{\Psi}_r\right) = \frac{p(\boldsymbol{\zeta}) W(\boldsymbol{\zeta}, \mathbf{\Psi}_r) H_\zeta(\boldsymbol{\zeta}, \mathbf{\Psi}_r)}{[1 + \Lambda(v_r) + \Lambda(v_s)] \cos\theta_r}, \tag{A9}$$

with

$$W(\boldsymbol{\zeta}, \mathbf{\Psi}_r) = \frac{\mathbf{U}_n \cdot \mathbf{U}_r}{z_n} \tag{A10}$$

which accounts for projection onto the receiver direction,

$$H_\zeta(\boldsymbol{\zeta}, \mathbf{\Psi}_r) = \Upsilon(\mathbf{U}_n \cdot \mathbf{U}_r) \tag{A11}$$

which accounts for not seeing the backside of waves, where Υ is the Heaviside function, and where

$$\begin{aligned} \Lambda\left(v\right) &= \frac{\exp(-v^2) - v_r\sqrt{\pi}\mathrm{erfc}(v)}{2v\sqrt{\pi}}, \quad v = \frac{\cot(\theta)}{\sqrt{2}\sigma(\phi)} \\ \sigma\left(\phi\right) &= \sqrt{\sigma_x^2 \cos^2\phi + \sigma_y^2 \sin^2\phi}. \end{aligned} \tag{A12}$$

Equation A12 applies to receiver ($\Lambda\left(v_r\right)$) or source ($\Lambda\left(v_s\right)$) elevation and is a result of the integration of the Smith [23, 24] height shadowing function. In these expressions $\mathbf{U_n}$ is the Cartesian surface facet normal unit vector, $\mathbf{U_r}$ is the surface to receiver unit vector, z_n is the zenith component of $\mathbf{U_n}$, and finally, $r\left(\mathbf{\Psi}_s, \mathbf{\Psi}_r\right)$ is the Fresnel reflection coefficient.

Although equation A8 is applicable to a point source, it has been shown by Ross et al. [3] that using the sun's irradiance and center position produces an error smaller than 1% on the resulting observed reflected radiance for any slope variance as long as the sun is more than 10° above the horizon.

Since the BRDF model uses geometrical optics as one of its premises, and because viscosity damping does not permit water surface structures to become much smaller than half a millimeter, the model can be used up to the far infrared. This approximation is adequate for most of the spectral domain covered by MODTRAN and by the validation measurements presented here.

Acknowledgments

The authors would like to thank the ONERA for generously providing their measurements for this validation. Special thanks to Sandrine Fauqueux and Karine Caillault (ONERA) for answering questions about the data and to Stéphane Langlois (ONERA) for enlightening discussions on the calibration uncertainties. We would also like to underline the notable contributions of Gail Anderson (US Air Force Research Laboratories) for her support and management and Alexander Berk (Spectral Sciences Inc.) for his great help in implementing the BRDF in MODTRAN and for his invaluable scrutiny in reviewing initial drafts of this paper.

References

1. A. Berk, G. P. Anderson, P. K. Acharya, L. S. Bernstein, L. Muratov, J. Lee, M. Fox, S. M. Adler-Golden, J. H. Chetwynd, M. L. Hoke, R. B. Lockwood, J. A. Gardner, T. W. Cooley, C. C. Borel, and P. E. Lewis, "MODTRAN 5: a reformulated atmospheric band model with auxiliary species and practical multiple scattering options: update," Proc. SPIE **5806**, 662–667 (2005).
2. A. Berk, L. S. Bernstein, and D. C. Robertson, "MODTRAN: A moderate resolution model for LOWTRAN7," Tech. Rep. GL-TR-89-0122, Air-Force Geophysics Lab., Bedford, MA (1989).
3. V. Ross, D. Dion, and G. Potvin, "Detailed analytical approach to the gaussian surface bidirectional reflectance distribution function specular component applied to the sea surface," J. Opt. Soc. Am. A **22**, 2442–2453 (2005).
4. V. Ross and D. Dion, "Sea surface slope statistics derived from Sun glint radiance measurements and their apparent dependence on sensor elevation," J. Geophys. Res. (Oceans) **112**, C09015 (2007).
5. K. Stamnes, S.-C. Tsay, K. Jayaweera, and W. Wiscombe, "Numerically stable algorithm for discrete-ordinate-method radiative transfer in multiple scattering and emitting layered media," Appl. Opt. **27**, 2502–2509 (1988).
6. P. K. Acharya, A. Berk, G. P. Anderson, G. P. Anderson, N. F. Larsen, S. Tsay, and K. H. Stamnes, "MODTRAN4: multiple scattering and bidirectional reflectance distribution function (BRDF) upgrades to MODTRAN," Proc. SPIE **3756**, 354–362 (1999).
7. J. L. Forand, "The L(W)WKD marine boundary layer model - version 7.09," Tech. Rep. 1999-099, Defence Research Establishment of Valcartier (DREV), Valcartier, Quebec, Canada (1999).
8. J. Piazzola, F. Bouchara, G. de Leeuw, and A. M. J. van Eijk, "Development of the Mediterranean extinction code (MEDEX)," Opt. Eng. **42**, 912–924 (2003).

9. L. Gardenal and D. Dion, "Aerosol Optical Properties Code (AeroProC)," Tech. rep. (2006). (available via Email by submitting request to the Authors).
10. S. G. Gathman, G. Deleeuw, K. L. Davidson, and D. R. Jensen, eds., *The naval oceanic vertical aerosol model* (1990).
11. S. G. Gathman, "Optical properties of the marine aerosols as predicted by the navy aerosol model," Opt. Eng. **22**, 57–62 (1983).
12. T. Saemundsson, "Atmospheric Refraction," Sky and Telescope **72**, 70–+ (1986).
13. T. Elfouhaily, B. Chapron, K. Katsaros, and V. D., "A unified directional spectrum for long and short wind-driven waves," J. Geophys. Res. **102**, 15781–15796 (1997).
14. J. A. Shaw, D. Cimini, E. R. Westwater, Y. Han, H. M. Zorn, and J. H. Churnside, "Scanning Infrared Radiometer for Measuring the Air -Sea Temperature Difference," Appl. Opt. **40**, 4807–4815 (2001).
15. A. Goroch, S. Burk, and K. L. Davidson, "Stability effects on aerosol size and height distributions," Tellus **32**, 245–+ (1980).
16. G. Tedeschi and J. Piazzola, "Development of a 2D marine aerosol transport model: Application to the influence of thermal stability in the marine atmospheric boundary layer," Atmospheric Research **101**, 469–479 (2011).
17. P. A. Hwang and O. H. Shemdin, "The dependence of sea surface slope on atmospheric stability and swell conditions," J. Geophys. Res. **93**, 13903–13912 (1988).
18. J. A. Shaw and J. H. Churnside, "Scanning-laser glint measurements of sea-surface slope statistics," Appl. Opt. **36**, 4202–4213 (1997).
19. C. Cox and W. Munk, "Measurement of the roughness of the sea surface from photographs of the sun glitter," J. Opt. Soc. Am. **44**, 838–850 (1954).
20. C. Cox and W. Munk, "Statistics of the sea surface derived from sun glitter," J. Mar. Res. **13**, 198–227 (1954).
21. Y. Liu, X.-H. Yan, and P. A. Hwang, "The probability density function of the ocean surface slopes and its effects on radar backscatter," J. Phys. Oceanogr. **27**, 782–797 (1997).
22. W. J. Plant, "A new interpretation of sea-surface slope probability density functions," J. Geophys. Res. **108**, 3295–3298 (2003).
23. B. G. Smith, "Lunar surface roughness, shadowing and thermal emission," J. Geophys. Res. **72**, 4059–4067 (1967).
24. B. G. Smith, "Geometrical shadowing of a random rough surface," IEEE Trans. Ant. Prop. **15**, 668–671 (1967).

Table 1. **Parameters for selected cases.**[a]

	ATAL 89	ATAL 95	ATAL 107	ATAL 109	ATAL 145	ATAL 64
Type	Off glint	Off glint	Off glint	Off glint	Glint	Glint
Date	May 23	May 23	May 23	May 23	May 28	May 22
Time (UT)	6:30:06	8:36:43	16:58:48	17:20:13	5:12:24	5:52:55
Band	BIII	BII	BII & BIII	BII & BIII	BII	BII
Air temp. (°C)	17.5	17.5	18.0	18.0	16.9	17.8
Sea temp. (°C)	17.8	17.7	17.6	17.7	17.1	17.56
Wind speed (m/s)	2.5	1.5	4.5	2.7	1.5	5.6
Rel. wind dir. (°)	137.0	108.9	149.0	-4.0	-92.9	38.0
Sun elev. (°)	24.12	47.13	19.87	16.02	10.86	17.20
Rel. sun azim. (°)	-158.55	-66.44	94.41	-79.25	-1.12	2.7
Visibility (km)	50.0	50.0	36.86	28.29	18.5	50.0
Rel. hum. (%)	74.0	78.0	89.0	88.0	89.0	67.0
Cloud	none	none	none	none	cirrus[b]	none

[a]Cases are in same order as they appear in the text.

[b]Standard MODTRAN, 1.8 km thickness.

List of Figure Captions

Fig. 1. Synthetic color background generated using MODTRAN (left) and the difference in path (atmospheric) radiance for the same scene from using a fully coupled BRDF as the bottom boundary condition instead of a Lambert surface with equivalent albedo.

Fig. 2. Band II camera response with no filter installed (full line) and with the N23 filter used for solar glint images (dotted line)

Fig. 3. Band III camera with LP11 filter installed

Fig. 4. Sea slope variances derived from the Elfouhaily et al. wave spectrum plotted against wind speed.

Fig. 5. Variation in modeled radiance when taking into account wind speed and slope variance model variability for case 108 (trial 1262) in the BIII band. Percentile differences from radiance measurments are also plotted in lower pane.

Fig. 6. Vertical profiles averaged in azimuth for all non-glint case. From top to bottom: ATAL 89 (trial 1116) in band BIII, ATAL 95 (trial 1159) in band BII, ATAL 107 (trial 1255) in band BII (left) and BIII (right), ATAL 109 (trial 1267) in band BII (left) and BIII (right).

Fig. 7. Vertical profile (A) and horizontal profile (B) obtained for glint case ATAL 145 (trial 1416) in band BII. The vertical profile is averaged on zone A of the reference image (top) while the horizontal profile is averaged on zone B. The sun is located at azimuth 0°.

Fig. 8. Vertical profile (A) and horizontal profile (B) obtained for glint case ATAL 64 (trial 902) in band BII. The vertical profile is averaged on zone A of the reference image (top) while the horizontal profile is averaged on zone B. The sun is located at azimuth 0°.

Fig. 9. Coordinate system and representation of relevant quantities: $\mathbf{U}_n$, facet Cartesian normal unit vector; $\mathbf{U}_r$, receiver Cartesian unit vector; $\mathbf{U}_s$, source Cartesian unit vector; ω, reflection angle; θ_i, zenith angle of $\mathbf{U}_i$ vector ($i = n, r, s$); ϕ_i, azimuth angle of $\mathbf{U}_i$ vector ($i = n, r, s$) from upwind direction ($\mathbf{W}$); ζ_x, facet slope in the upwind ($\mathbf{W}$) direction; ζ_y, facet slope in the cross-wind direction.

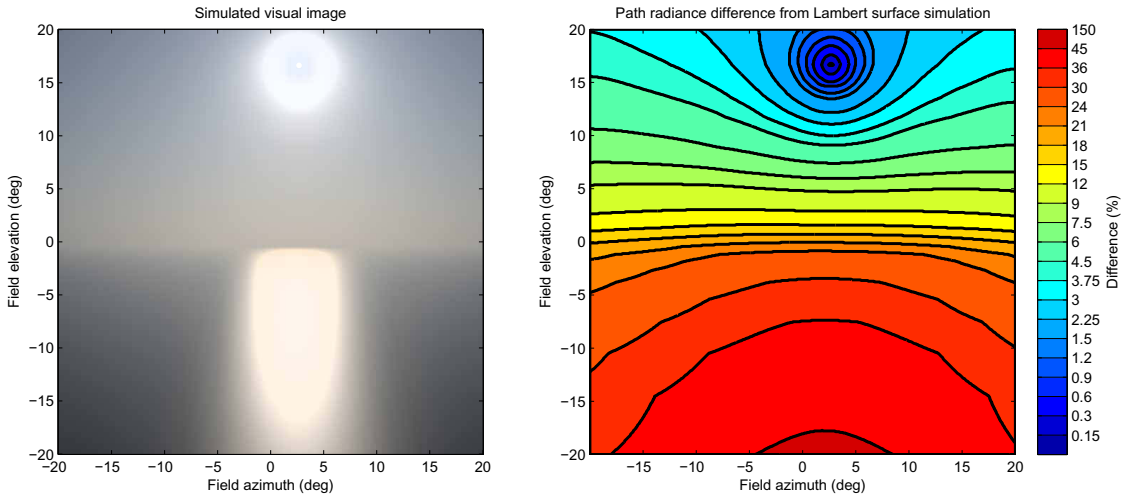

Fig. 1. Synthetic color background generated using MODTRAN (left) and the difference in path (atmospheric) radiance for the same scene from using a fully coupled BRDF as the bottom boundary condition instead of a Lambert surface with equivalent albedo.

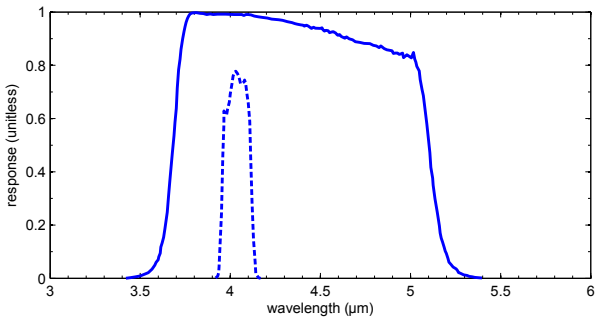

Fig. 2. Band II camera response with no filter installed (full line) and with the N23 filter used for solar glint images (dotted line)

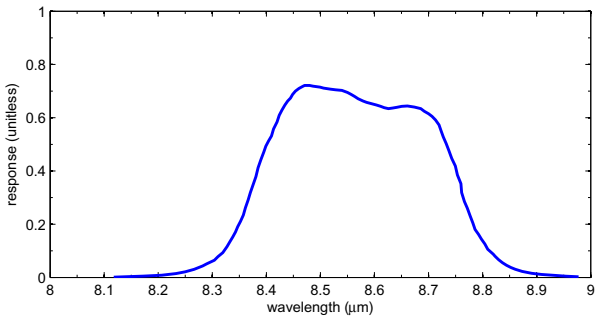

Fig. 3. Band III camera with LP11 filter installed

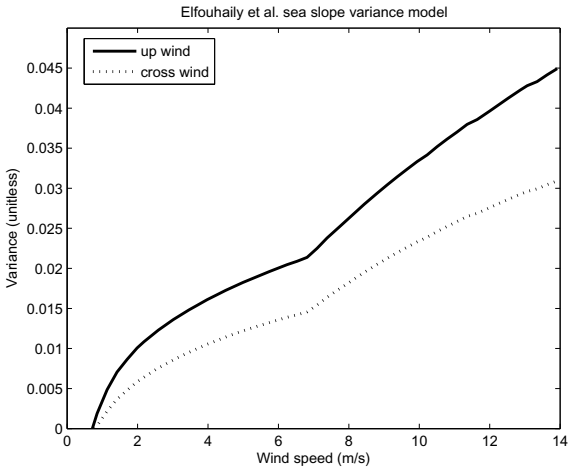

Fig. 4. Sea slope variances derived from the Elfouhaily et al. wave spectrum plotted against wind speed.

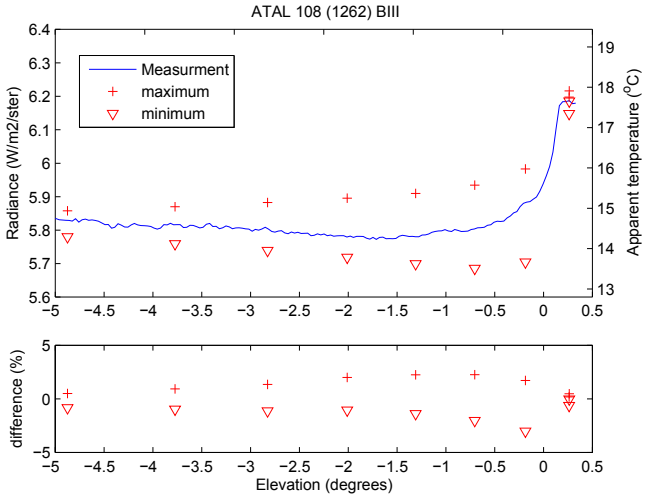

Fig. 5. Variation in modeled radiance when taking into account wind speed and slope variance model variability for case 108 (trial 1262) in the BIII band. Percentile differences from radiance measurments are also plotted in lower pane.

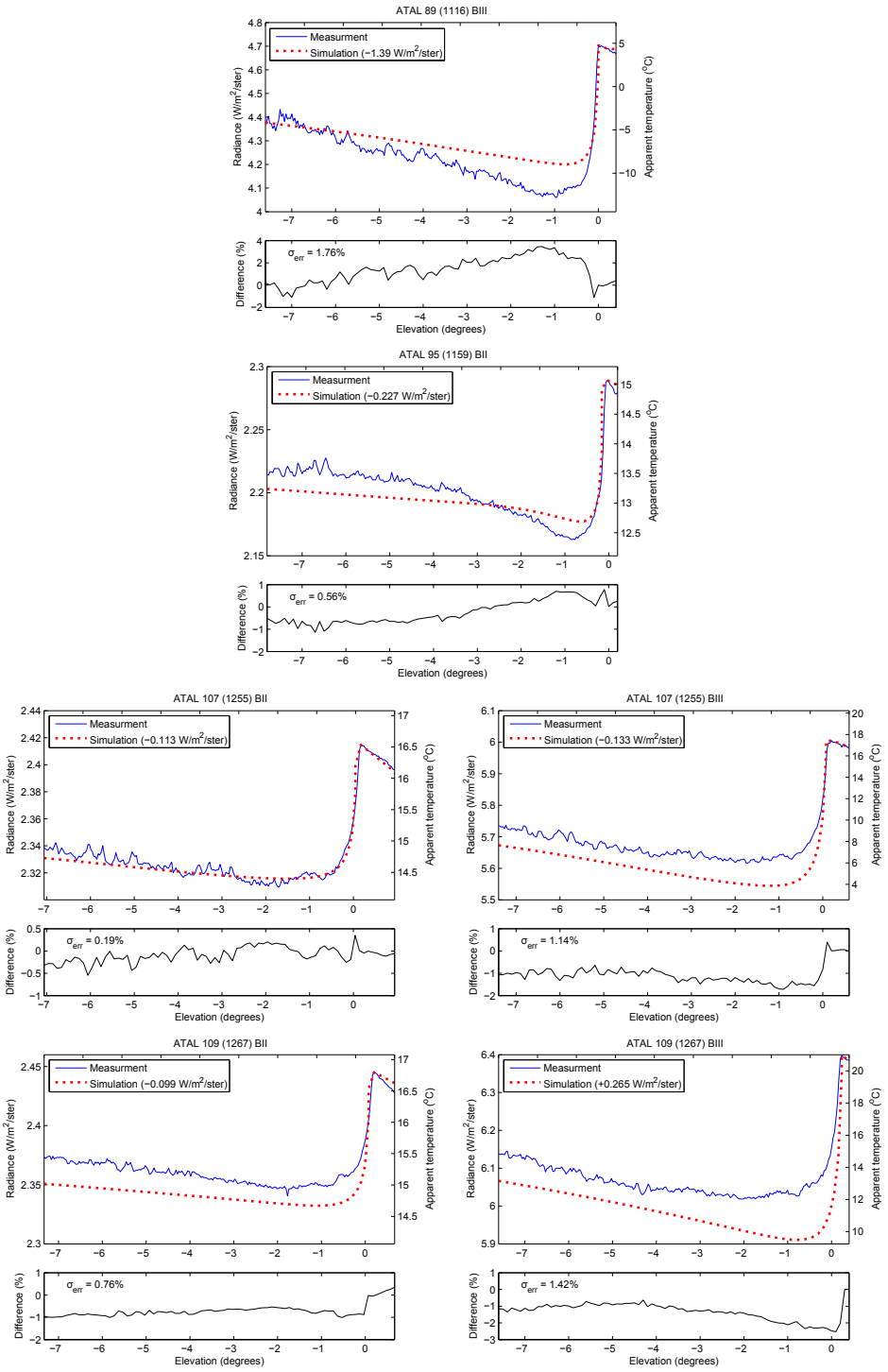

Fig. 6. Vertical profiles averaged in azimuth for all non-glint case. From top to bottom: ATAL 89 (trial 1116) in band BIII, ATAL 95 (trial 1159) in band BII, ATAL 107 (trial 1255) in band BII (left) and BIII (right), ATAL 109 (trial 1267) in band BII (left) and BIII (right).

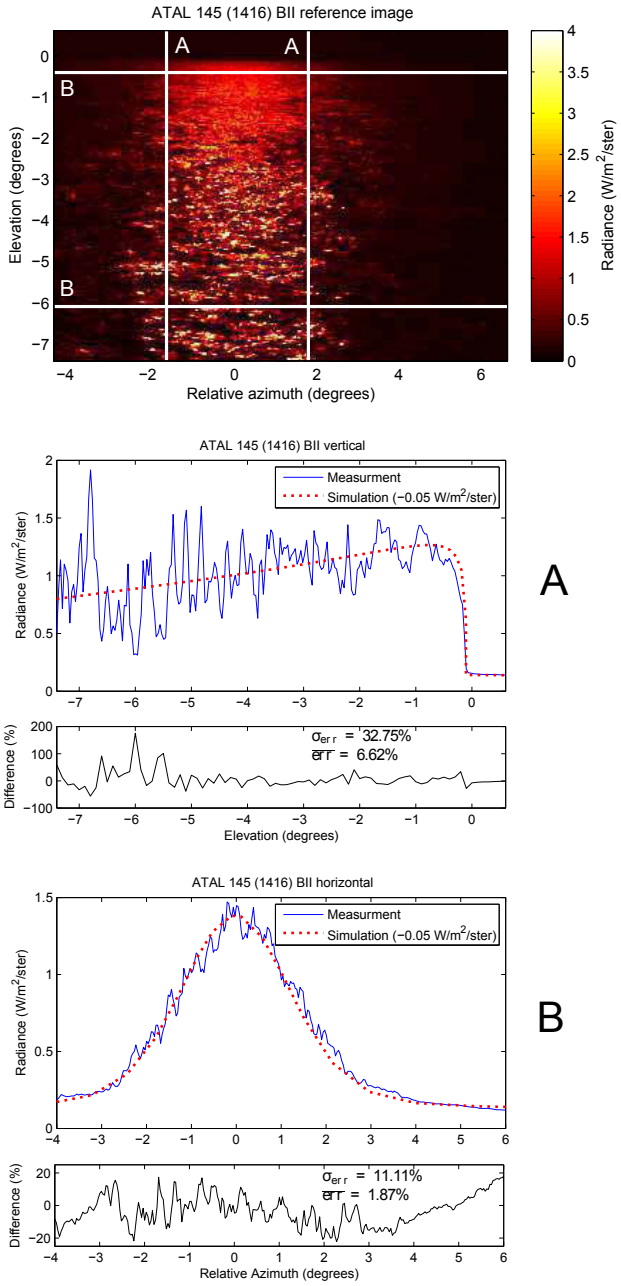

Fig. 7. Vertical profile (A) and horizontal profile (B) obtained for glint case ATAL 145 (trial 1416) in band BII. The vertical profile is averaged on zone A of the reference image (top) while the horizontal profile is averaged on zone B. The sun is located at azimuth 0°.

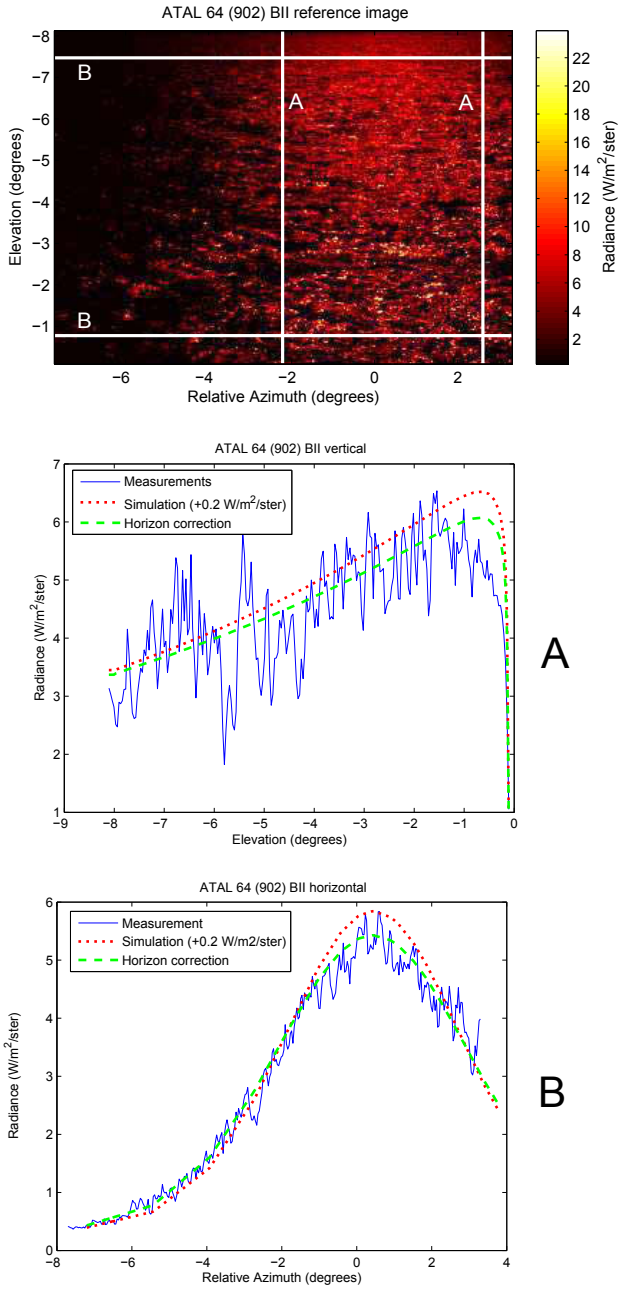

Fig. 8. Vertical profile (A) and horizontal profile (B) obtained for glint case ATAL 64 (trial 902) in band BII. The vertical profile is averaged on zone A of the reference image (top) while the horizontal profile is averaged on zone B. The sun is located at azimuth 0°.

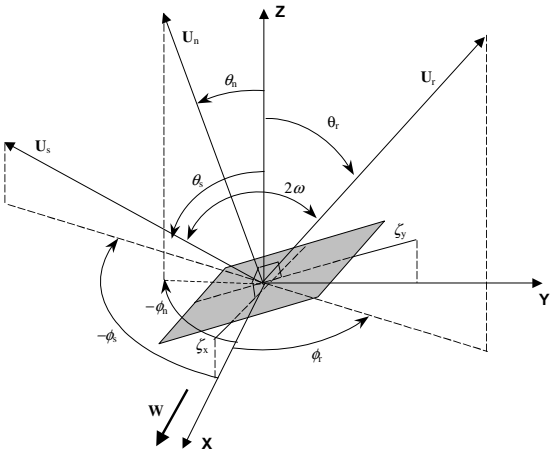

Fig. 9. Coordinate system and representation of relevant quantities: $\mathbf{U}_n$, facet Cartesian normal unit vector; $\mathbf{U}_r$, receiver Cartesian unit vector; $\mathbf{U}_s$, source Cartesian unit vector; ω, reflection angle; θ_i, zenith angle of $\mathbf{U}_i$ vector ($i = n, r, s$); ϕ_i, azimuth angle of $\mathbf{U}_i$ vector ($i = n, r, s$) from upwind direction ($\mathbf{W}$); ζ_x, facet slope in the upwind ($\mathbf{W}$) direction; ζ_y, facet slope in the cross-wind direction.